Pt supported and carbon coated Bi_2MoO_6 composite for enhanced 2, 4–dibromophenol degradation under visible–light irradiation: Insight into band gap structure and photocatalytic mechanism

Juan Wu[a], Yuying Sun[a], Chunhao Gu[b], Ting Wang[a], Yanjun Xin[a], Chao Chai[a], Chunyue Cui[a], Dong Ma[a,*]

[a] Rural Environmental Engineering Center of Qingdao, College of Resource and Environment, Qingdao Agricultural University, Qingdao 266109, China
[b] Department of Ecosystem Science and Management, University of Wyoming, Laramie, WY 82071, United States

ARTICLE INFO

ABSTRACT

This study aims to reveal the visible–light photocatalytic performance of Pt supported and carbon coated Bi_2MoO_6 (Pt/C@Bi_2MoO_6) composite on the degradation of aquatic 2,4–dibromophenol (DBP) pollutant. The surface structure analysis shows that Pt and carbon layer can tightly bind to the surface of Bi_2MoO_6 with the chemical bonds, and hybrid the original band gap to generate new impurity levels to enhance the visible–light utilization efficiency. The carbon layer has excellent conductivity to transformation electrons from valence band (VB) site, and the supported Pt atoms on carbon layer generate a plasma electron field to enhance the reductive activity on conduction band (CB) site. The Pt/C@Bi_2MoO_6 composite shows more efficient and reliable abilities in DBP photocatalytic degradation, and the debromination and oxidization processes are performed separately on CB and VB site, respectively. The DBP debromination proceeds by electrons in the CB site in priority to generate non–brominated intermediate products, and then the oxidization and mineralization procedures start by hydroxide radicals in the VB site to finish the complete degradation of DBP. This research reveals the important roles of Pt and carbon layer in band gap structure modification and photocatalytic activity improvement, exhibiting a new insight to design an efficient and stable photocatalyst for persistent organic pollutant degradation under visible–light irradiation.

1. Introduction

The halophenols are carcinogenic and toxic for living being, and among the most refractory organic substance in surface environment [1,2]. Variety of techniques for halophenols treatment have been developed in biodegradation, adsorption or chemical oxidation, however, they suffer from low degradation rate, secondary pollution or expensive expense [3–5]. Photocatalytic degradation has emerged as a significant technology to degradate halophenols due to its low cost with renewable sunlight and almost complete mineralization, and the bromophenols, such as bromophenol (BP), 2,4–dibromophenol (DBP), 2,4,6–tribromophenol (TBP) and tetrabromobisphenol A (TBBPA), have frequently been used as targets to evaluate the photocatalytic activity in water decontamination [6–8].

In the photocatalytic process, there are two major oxidative species, hydroxide ($\cdot OH$) and superoxide anion ($\cdot O_2^-$) radicals, which have been thought as the dominant radicals in halophenols degradation by oxidative procedures [9]. In the DBP and TBP photocatalytic degradation by TiO_2/UV [10] and FeOOH–$ZnIn_2S_4$ [11], respectively, the generated $\cdot OH$ radicals were suggested playing a leading role in debromination and degradation processes. The $\cdot O_2^-$ radicals were also identified as major contributors in degradation and mineralization process of BP by CeO_2 [12] or Mn_3O_4/ZnO [13] photocatalysts, as well as photodegradation of TBBPA by metalloporphyrins photocatalyst [7]. In other previous results, reductive progress was assumed as the major force for cleavage of C—Br bonds throughout the bromophenols degradation [14–16]. In order to remove bromophenols more efficiently, therefore, either the oxidative or reductive progress can be attributed the cleavage of C—Br bonds should be made clear in the debromination process.

According to the previous study, a variety of supported noble metal like Pt has been used to enhance the photo-activities, and the supported Pt had large work function, surface plasmon resonance and effective ability to capture the electrons to assist showing higher photocatalytic performance [17]. Li et al. [18] found that Pt acted as electron sinks in Pt—TiO_2 to store the excess electrons in conduction band to enhance

decomposition of perfluorooctanoic acid. Tanaka et al. [19] reported that a Pt/Au/WO$_3$ photocatalyst can efficiently transfer electrons and generate H$_2$ by the reduction over Pt. Thus, we conclude that Pt could be an electron acceptor and provide more reductive ability in the conduction band site. Our present works reported a carbon coated Bi$_2$MoO$_6$ (C@Bi$_2$MoO$_6$) photocatalyst [20,21], in which the coated carbon on the surface of Bi$_2$MoO$_6$ acted as an electron mediator to form the charge transmission-bridge for efficient separation of photoexcited holes and electrons. The supported Pt may be conceived of the electron acceptor to assist charge transmission from valance band of the C@Bi$_2$MoO$_6$.

In this study, we prepared a new type of Pt supported and carbon coated Bi$_2$MoO$_6$ (Pt/C@Bi$_2$MoO$_6$) composite, in which Pt nanoparticles were loaded on the surface of the carbon layer. DBP was employed to evaluate the photocatalytic oxidative and reductive performance of the Pt/C@Bi$_2$MoO$_6$ composite. We investigated the roles of Pt and carbon layer played in the photocatalytic procedure and also discussed the mechanism in debromination and degradation of DBP over Pt/C@Bi$_2$MoO$_6$ composite.

2. Experimental

2.1. Synthesis of Pt/C@ Bi$_2$MoO$_6$ composite photocatalyst

All of the chemicals in the present work were analytic grade without further purification, and deionized (DI) water was used throughout the experiments. The synthesis steps of Pt/C@Bi$_2$MoO$_6$ composite are shown in Scheme 1. Bi$_2$MoO$_6$ photocatalyst was prepared by a hydrothermal method (Scheme 1, Step 1) in our previous work [22]. In a typical procedure, 2.0 mmol of Bi(NO$_3$)$_3$·5H$_2$O and 0.143 mmol of (NH$_4$)$_6$Mo$_7$O$_{24}$·4H$_2$O were dissolved in 10 mL (2.0 M) HNO$_3$ and 10 mL DI water under stirring for 20 min, respectively. The Bi(NO$_3$)$_3$·5H$_2$O solution was then dropped into the (NH$_4$)$_6$Mo$_7$O$_{24}$·4H$_2$O solution under constant stirring for 60 min, and the pH of the suspension was adjusted to neutral (pH 7.0 ± 0.05) by ammonium hydroxide. The obtained mixture was transferred into a Teflon–lined stainless steel autoclave (100 mL) and maintained 180 °C for 12 h. The obtained products were washed with DI water and absolute ethanol several times, and the pure Bi$_2$MoO$_6$ photocatalyst was then collected by drying in vacuum at 60 °C for 8 h for further use.

Carbon–coated Bi$_2$MoO$_6$ (C@Bi$_2$MoO$_6$) was synthesized via a hydrothermal method (Scheme 1, Step 2) [20]. 0.1 g of Bi$_2$MoO$_6$ was added to 80 mL glucose solution (30 mg/L) under vigorous stirring, and

the mixture was transferred into Teflon–lined autoclave and heated at 180 °C for 6 h. The product of C@Bi$_2$MoO$_6$ was obtained after being washed and dried. Pt supported and carbon coated Bi$_2$MoO$_6$ (Pt/C@Bi$_2$MoO$_6$) were prepared by the following procedures (Scheme 1, Step 3). A certain amount of H$_2$PtCl$_6$ (4 mM), 2.5 mL NaBH$_4$ sulution (0.1 M) and 0.2 g as–prepared C@Bi$_2$MoO$_6$ composite were added to 100 mL DI water, and the mixture was treated by ultrasonic processing for 30 min to obtain the Pt/C@Bi$_2$MoO$_6$ composite. Samples with different ratio of Pt to Bi$_2$MoO$_6$ were obtained with labeled as x% Pt/C@Bi$_2$MoO$_6$, where x standed for the Pt/Bi$_2$MoO$_6$ molar ratio in the composite.

2.2. Characterization

X–ray Powder Diffraction (XRD) was performed on a D8 Advance diffract meter (Bruker, Germany) using Ni-filtered Cu *Kα* radiation (=1.5418 Å) at 60 kV and 60 mA over the 2θ range of 10–80°. The surface morphologies and compositions of photocatalysts were examined using a scanning electron microscope (SEM, JEOL 7500F) combined with energy dispersive X–ray spectrometer (EDX). The ultra–structure of each sample was observed by a high–resolution transmission emission microscopy (HRTEM, JEOL, JEM 2100). Infrared spectra were recorded by a Fourier transform infrared spectrometer (FTIR, Nicolet Avatar 370) using KBr as background. X–ray photoelectron spectroscopy (XPS) measurements were obtained using an ESCALAB 250 spectrometer (Thermo Fisher Scientific, UK) with non––monochromatic Al K X–rays (1486.6 eV). The binding energy was calibrated by taking the C 1s peak of contaminant carbon as a reference at 284.6 eV. UV–vis diffuse reflectance spectra (DRS) were carried out with a UV–vis spectrophotometer (TU–1901) using BaSO$_4$ as reference. The electrochemical workstation (CHI–660B) was used to measure the photocurrent intensities, electrochemical impedance spectra and Mott–Schottky plots of the samples with 0.1 M Na$_2$SO$_4$ as the electrolyte at a frequency of 1 KHz. The photocatalyst powder were fixed on the working electrode by the conductive adhesive, and a standard three–electrode cell was used in the photoelectric measurement, with saturated calomel electrode (SCE) and Pt plate as the reference and counter electrodes, respectively. Photoluminescence (PL) spectra of the samples were collected on a fluorescence spectrometer (Hitachi F–4600), and the time–resolved fluorescence emission decay measurements were obtained using a Fluorescence Spectrometer (Edinburgh FL–920) with the excitation wavelength of 340 nm. The radical species were detected by using the electron spin resonance (ESR) spectrometer (Bruker EMX EPR) with the center field of 3367G and the microwave

Scheme 1. Synthesis steps of Pt/C@Bi$_2$MoO$_6$ composite. Step 1: hydrothermal process of Bi$_2$MoO$_6$ synthesis from Bi(NO$_3$)$_3$·5H$_2$O and (NH$_4$)$_6$Mo$_7$O$_{24}$·4H$_2$O; Step 2: hydrothermal process of C@Bi$_2$MoO$_6$ preparation using glucose as carbon source; Step 3: Ultrasonic process with the presence of H$_2$PtCl$_6$ and NaBH$_4$ to obtain the Pt/C@Bi$_2$MoO$_6$ composite.

power of 21.45–21.95 mW.

2.3. Evaluation of photocatalytic activity

The photocatalytic activities of as–prepared samples were evaluated in terms of the photocatalytic degradation of 2,4–dibromophenol (DBP), which was carried out at ambient temperature in a continuous flow reactor. The photocatalyst of 0.1 g was put into 100 mL DBP solution (10 mg/L), and a 500 W Xe lamp (with the incident radiation of 3.2×10^{-7} Es^{-1} cm^{-2}) was used as visible–light source. The distance between the Xe lamp and the reactor was 25 cm, and the UV light portion was filtered by a 420 nm cut–off filter. Before the photocatalytic reaction, the mixture was stirred in the dark for 30 min to obtain the equilibrium adsorption–desorption. At certain time, suspension was partly taken out from the mixture and immediately centrifuged. The obtained solution was analyzed with the concentration of DBP and bromide ions. The concentration of DBP was determined by high performance liquid chromatography (HPLC, Shimadzu, LC–20A) using a Inertsil column (4.6 mm × 150 mm) with the column temperature was 30 °C with the detection wavelength of 280 nm [23,24]. The intermediate substances were measured by HPLC/MS (LTQ-Orbitrap) analysis. The concentration of bromide ion ([Br$^-$]) in solution after DBP photocatalytic degradation was detected by Ion Chromatography (Dion, ICS–90), and the [Br$^-$] standard curve was diluted sequentially from 100 mg/L KBr solution. The corresponding total organic carbon (TOC) contents of the solutions were determined by a TOC analyzer (Germany Multi–N/C 2000). To detect the active species during photocatalytic reactivity, sacrificial agents were used to capture different active species. The hole (h$^+$), electron (e$^-$), hydroxyl radical (·OH) and superoxide anion radical (·O$_2^-$) were captured by sodium oxalate (5 mM), Cr (VI) (0.5 mM), isopropanol (IPA, 5 mM) and 4–Hydroxy–2,2,6,6–tetramethyl piperidinyloxy (TEMPOL, 2 mM), respectively [25,26].

3. Results and discussion

3.1. Crystal structure and morphology

Othorhombic Bi$_2$MoO$_6$ crystals are obtained both in C@Bi$_2$MoO$_6$ and Pt/C@Bi$_2$MoO$_6$ composites (Fig. 1A), and the main diffraction peaks of composites can be well indexed to the orthorhombic Bi$_2$MoO$_6$

(JCPDS No. 76–2388) [27]. The positions of the main characteristic peaks of Bi$_2$MoO$_6$ have no significantly change, indicating that the addition of C and Pt has scarcely changed the crystal structure of the bulk of Bi$_2$MoO$_6$. However, the intensities of the diffraction peaks of Bi$_2$MoO$_6$ become weaker, illustrating that the combination between Pt and C@Bi$_2$MoO$_6$ has decreased the diffractive efficiency of the bulk of Bi$_2$MoO$_6$ [28]. The peaks of C are not observed in the XRD patterns of the samples, suggesting the presence of amorphous carbon rather than crystalline structure in the C@Bi$_2$MoO$_6$ and Pt/C@Bi$_2$MoO$_6$ composites [20,21]. The characteristic peaks of Pt (JCPDS No. 04–0802) are observed in Fig. 1B magnified from Fig. 1A, such as the crystallographic planes of (111), (200) and (220) at the 2 theta of 39.7°, 46.2° and 67.4°, respectively [29].

The as–prepared Pt/C@Bi$_2$MoO$_6$ composite is composed of many irregular micro–scale nanosheets with the thickness of dozens of nanometers, which can be seen clearly in the typical SEM morphology of 2.0%Pt/C@Bi$_2$MoO$_6$ composite (Fig. 2A). The EDX spectrum of the 2.0%Pt/C@Bi$_2$MoO$_6$ composite (Fig. 2B) linked to SEM analysis shows that the elements of Bi, Mo, O, C and Pt have existed in the composite. The elemental mapping images is shown in Fig. 2C, and it can be observed that the Mo, Bi, C and Pt elements are distributed in the Pt/C@Bi$_2$MoO$_6$ composite in Fig. 2C1, C2, C3 and C4, respectively, which confirms the elemental composition of the Pt/C@Bi$_2$MoO$_6$ composite.

The ultra–structure of crystal lattice of the 2.0%Pt/C@Bi$_2$MoO$_6$ composite were obtained from the TEM and HRTEM images (Fig. 2D–F). We also can see many nanosheets in the microscope, and when edge of the namosheet is magnified enough, a carbon layer with a thickness of ~ 20 nm can be seen on the surface of the Bi$_2$MoO$_6$ nanosheets. Large amount of Pt nanoparticles disperse on the surfaces of C@Bi$_2$MoO$_6$, with a diameter of several nanometers (Fig. 2E). Furthermore, the distinct lattice fringes can be observed in the HRTEM of the Pt/C@Bi$_2$MoO$_6$ composite, as shown in Fig. 2F, and the interplanar spacings of 0.23 nm and 0.32 nm match with the crystallographic planes of Pt (111) and Bi$_2$MoO$_6$ (131), respectively [30,31]. It confirms that the Pt nanoparticles are completely reduced with ultrasound method, and they are combined tightly with the carbon layer on the surface of the bulk Bi$_2$MoO$_6$ nanosheet. The joint connections on the both sides of carbon layer with Bi$_2$MoO$_6$ nanosheet and Pt nanoparticles might provide increasingly opportunity for the interfacial charge transfer to improve the separation efficiency of photogenerated carriers.
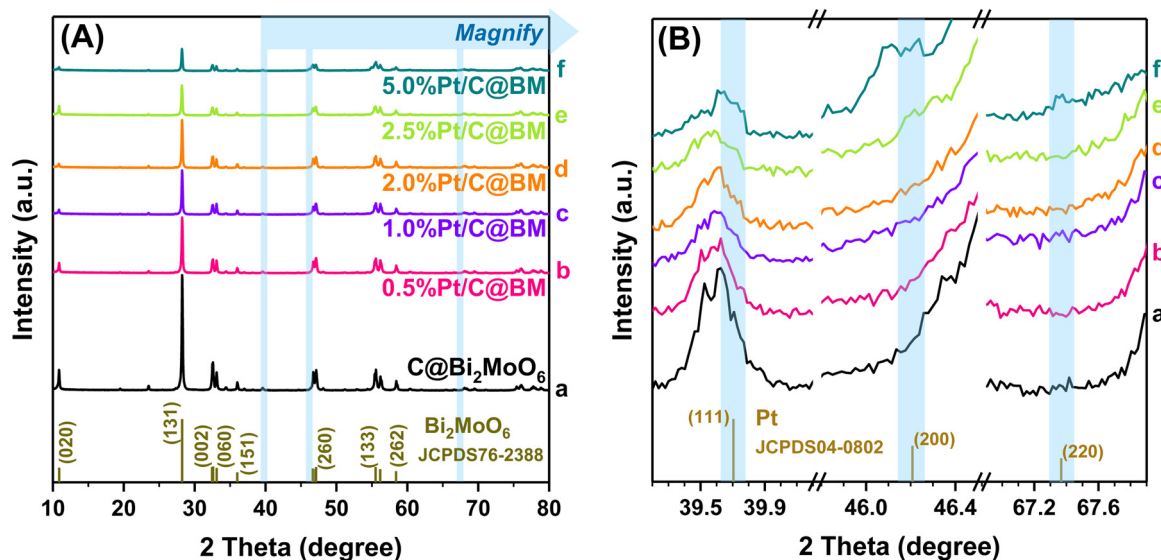

Fig. 1. Powder X–ray diffraction (XRD) patterns of C@Bi$_2$MoO$_6$ and Pt/C@Bi$_2$MoO$_6$ (BM) composites, (a) C@ Bi$_2$MoO$_6$, (b) 0.5%Pt/C@BM, (c) 1.0%Pt/C@BM, (d) 2.0%Pt/C@BM, (e) 2.5%Pt/C@BM and (f) 5.0%Pt/C@BM. The light blue areas in (A) are magnified to (B). (For interpretation of the references to colour in this figure legend, the reader is referred to the web version of this article.)
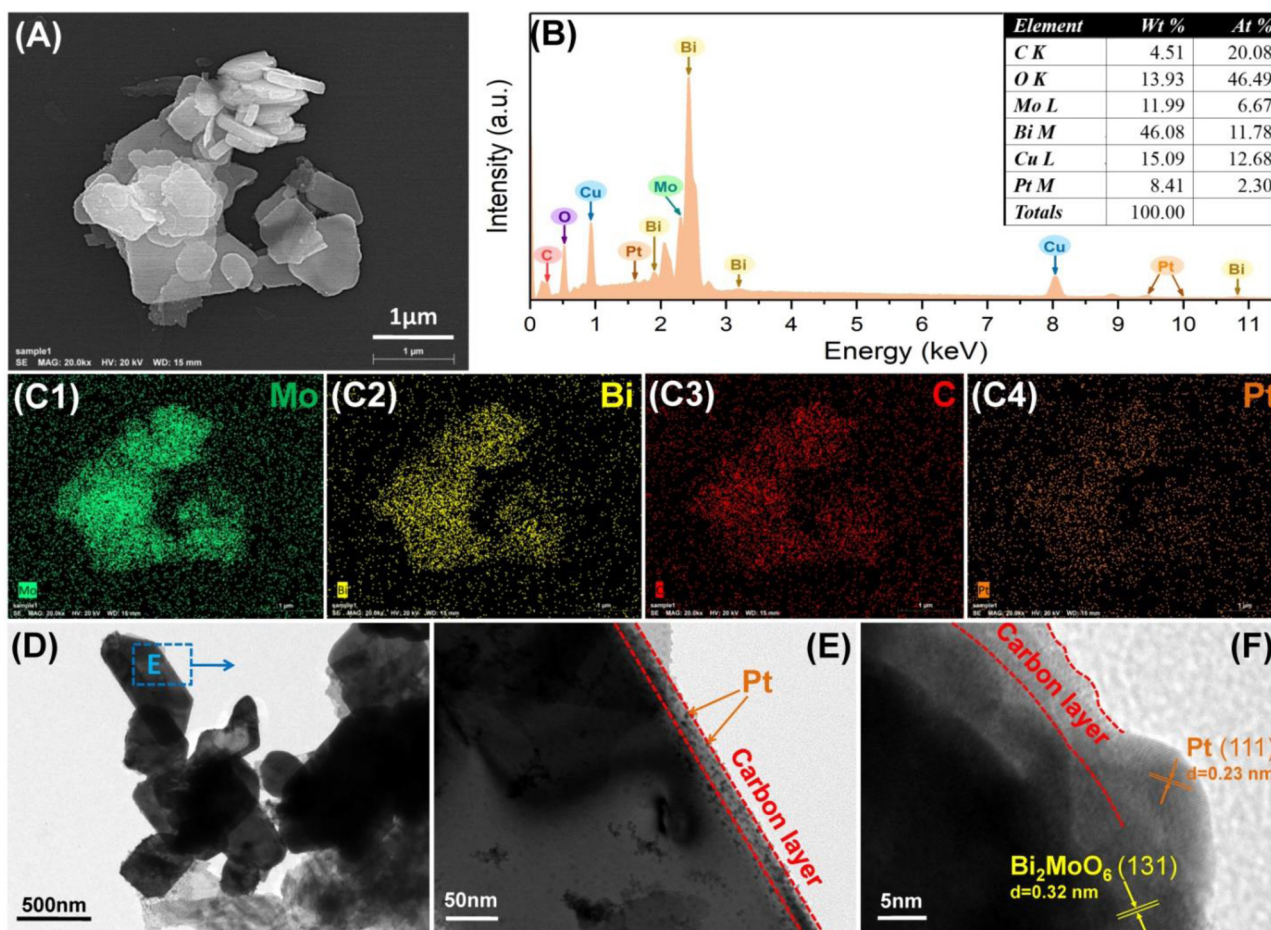
Fig. 2. SEM (A), EDX (B), elemental mapping (C), TEM (D and E) and HRTEM (F) images of 2.0%Pt/C@Bi$_2$MoO$_6$ composite, (C1) for Mo, (C2) for Bi, (C3) for C and (C4) for Pt, and the blue area in (D) is magnified to (E). (For interpretation of the references to colour in this figure legend, the reader is referred to the web version of this article.)

3.2. Surface structure and properties

Surface structure and properties of the photocataly play important roles on performance of the photodegradation activity. The FTIR spectra of 1.0%C@ Bi$_2$MoO$_6$ and 2.0%Pt/C@Bi$_2$MoO$_6$ composites are shown in Fig. 3A. The strong IR signal in the range of 400–900 cm^{-1} is appeared in 1.0%C@Bi$_2$MoO$_6$ and 2.0%Pt/C@Bi$_2$MoO$_6$, corresponding to the Bi−O, Mo−O stretching and Mo−O−Mo bridging stretching modes. The IR peaks at 450 cm^{-1} and 582 cm^{-1} are assigned to Bi−O deformation vibration and stretching vibration, respectively [32]. The IR peaks at around 722 cm^{-1} and 839 cm^{-1} are attributed to the asymmetric stretching mode of MoO$_6$ involving vibrations of the equatorial and apical oxygen atoms, respectively [23,33]. The FTIR peaks at 797 cm^{-1} can be assigned to the stretching mode of MoO$_6$ involving vibrations of the apical oxygen atoms [34]. It is noteworthy that peaks of 2.0%Pt/C@Bi$_2$MoO$_6$ at 1380 cm^{-1} are attributed to different vibration modes of O=C−O, and the peak appearing at 1635 cm^{-1} arises from C−C vibrations [32,35].

To better understand the chemical states of Bi, Mo, O, C and Pt elements in the Pt/C@Bi$_2$MoO$_6$ composite, the XPS technique was employed to identify the chemical states of Bi, Mo, O, C and Pt in the 2.0%Pt/C@Bi$_2$MoO$_6$ composite (Fig. 3B). The obtained spectrum for Bi 4f is shown in Fig. 3C. The presence of the doublet Bi 4f peaks indicates that bismuth existed in a single chemical state. The two peaks were relative to the binding energy of Bi 4f$_{7/2}$ and Bi 4f$_{5/2}$. Bi states can be divided into four peaks, and the two right peaks at 164.1 eV and 158.7 eV can be ascribed to the Bi^{3+} in Bi$_2$MoO$_6$ rhombohedron structures. The two left peaks centered at around 164.8 eV and 159.5 eV

are in agreement of the Bi^{3+} of Bi−O−C bonds in the carbon electron density, which further illustrates the existence of carbon layer on the surface of Bi$_2$MoO$_6$ nanosheets [36,37]. In Fig. 3D, the binding energies of 232.0 eV and 235.2 eV corresponded to the Mo 3d$_{5/2}$ and Mo 3d$_{3/2}$ peaks arising from a spin orbital interaction. The XPS spectrum of C 1s is shown in Fig. 3E. The asymmetric peaks around 284.4 eV is deconvoluted into four peaks at 287.3 eV, 284.9 eV, 284.4 eV and 283.6 eV. The peaks at 284.4 eV correspond to the C−C bonds for Pt/C@Bi$_2$MoO$_6$. The peak at 284.9 eV is ascribed to the Mo−O−C and Bi−O−C bonds formed between Bi$_2$MoO$_6$ and the carbon layer. The peaks at 287.3 eV and 283.6 eV are ascribed to the C−O and C=C bonds, respectively [21]. All the results indicate that metal−O−C bonds are formed at the interfaces between Bi$_2$MoO$_6$ and the carbon layer. As shown in Fig. 3F, the Pt 4f peaks centered at the range of 69.6 to 77.6 eV could be attributed to Pt 4f$_{5/2}$ and Pt 4f$_{7/2}$ of Pt, respectively, which confirmed that Pt existed in a form of metal state [23]. Furthermore, the Pt° 4f$_{5/2}$ and 4f$_{7/2}$ characteristic peaks are observed at 71.3 and 74.8 eV, and the peaks attributed to Pt^{2+} 4f$_{5/2}$ and 4f$_{7/2}$ are also found at 72.3 and 75.6 eV, and the two peaks at 74.4 and 77.2 eV are ascribed from the Pt^{4+} 4f$_{5/2}$ and 4f$_{7/2}$, respectively [38]. It could be concluded that the supported Pt was not all the Pt° after NaBH$_4$ reducing, and Pt had a metal state as well as the crystalline phase [39], which was also be detected by XRD patterns. Thus, it is suggested that Pt and carbon layer can tightly bind to Bi$_2$MoO$_6$ with the formation of C−O−Bi and C−O−Pt bonds on the surface of the composite.
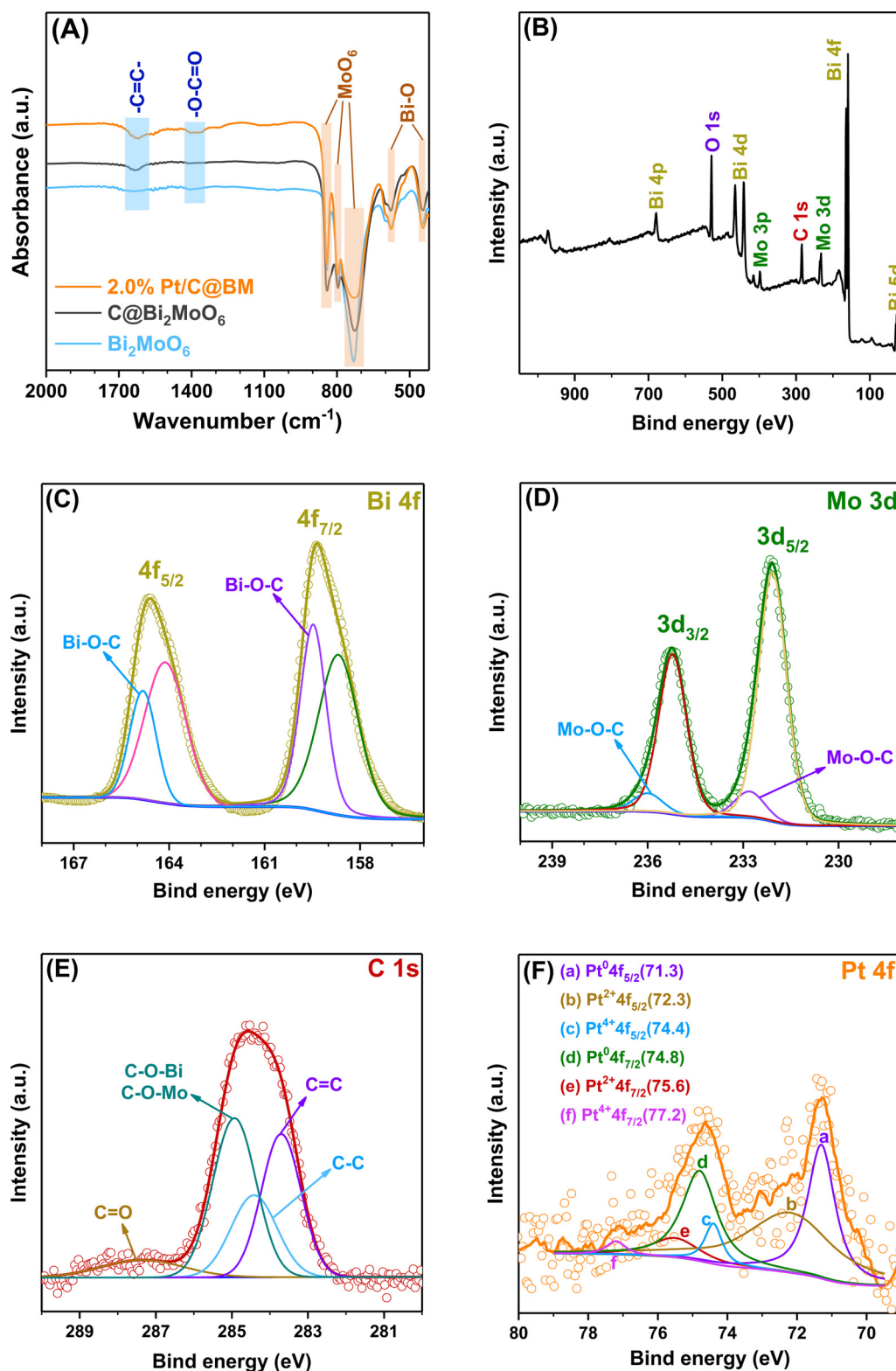
Fig. 3. FTIR spectra (A) of Bi_2MoO_6, $C@Bi_2MoO_6$ and 2.0%$Pt/C@Bi_2MoO_6$ (BM) composite, survey XPS spectrum of 2.0%$Pt/C@BM$ composite (B), and high–resolution XPS spectra of 2.0%$Pt/C@BM$ composite with Bi 4f (C), Mo 3d (D), C 1s (E) and Pt 4f (F).

3.3. Photoexcited properties and band structures

As is well–known, Bi_2MoO_6 is a photocatalyst drived by visible–light. The as–prepared pure Bi_2MoO_6 in this study has a wide absorption in visible–light region, as well as the $C@Bi_2MoO_6$ and $Pt/C@Bi_2MoO_6$ composite (Fig. 4A). Correspondingly, the band gap energy

(E_g) of the pure Bi_2MoO_6, $C@Bi_2MoO_6$ and $Pt/C@Bi_2MoO_6$ composite photocatalysts calculated according to *Kubelka–Munk* equation are 2.2 eV, 1.9 eV and 1.6 eV, respectively, as shown in Fig. 4B. It can be found that the E_g of Bi_2MoO_6 is narrow down after coating carbon on the surface (from 2.2 eV to 1.9 eV), and the E_g of $Pt/C@Bi_2MoO_6$ composite decreases to 1.6 eV after Pt was loaded on the surface. It
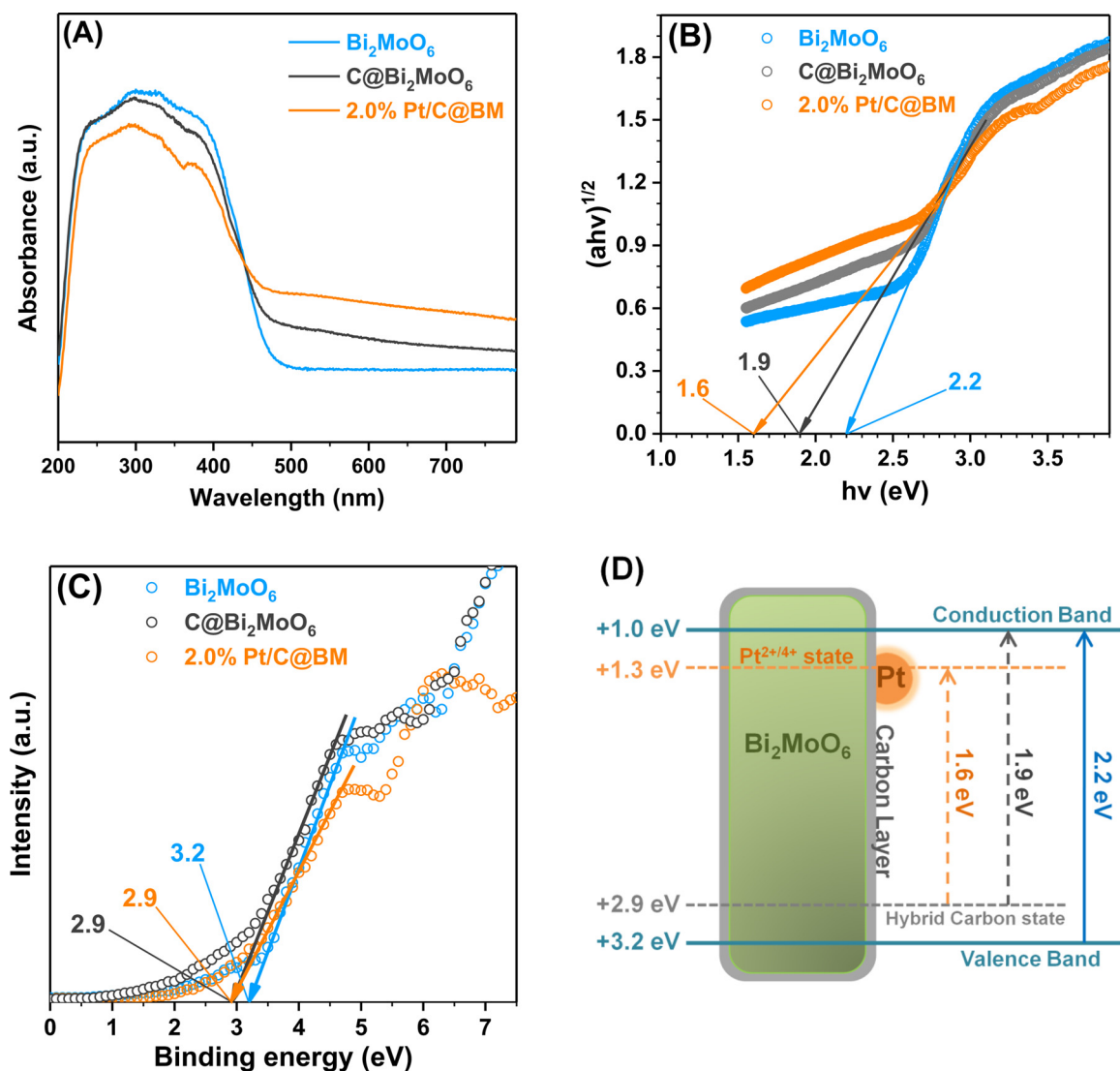
Fig. 4. (A) UV–Vis DRS curves of Bi_2MoO_6, $C@Bi_2MoO_6$ and 2.0%Pt/C@Bi_2MoO_6 (BM) composite, (B) the $(ah\nu)^{1/2} \sim h\nu$ plots of Bi_2MoO_6 and 2.0%Pt/C@BM composite, (C) valence band XPS curves of Bi_2MoO_6 and 2.0%Pt/C@BM composite, and (D) the possible band structure of the 2.0%Pt/C@BM composite. (For interpretation of the references to colour in the text, the reader is referred to the web version of this article.)

suggests that the introduction of carbon and Pt have significant effects on narrowing the E_g and thus, increasing the visible–light absorption. The valence band XPS of the as–prepared photocatalysts were measured to find out the positions of the valence band edges (E_{VB}) of the photocatalysts (Fig. 4C). The C@Bi_2MoO_6 and Pt/C@Bi_2MoO_6 composite have the same position of 2.9 eV (vs. NHE), with the 0.3 eV shift from the E_{VB} position of the pure Bi_2MoO_6 (3.2 eV vs. NHE).

Furthermore, the Mott-Schottky plots of the pure Bi_2MoO_6, C@Bi_2MoO_6 and Pt/C@Bi_2MoO_6 (BM) composites were analyzed (Fig. S1). The Fermi level of C@Bi_2MoO_6 is smaller than the level of pure Bi_2MoO_6, indicating that the new impurity level has been generated under the original Fermi level, and the O 2p electronic orbit has been partially occupied by coated carbon with its s orbit [40,41]. This result completely agrees with the previous work [41]. For another, the Fermi level of 2.0%Pt/C@Bi_2MoO_6 is higher than that C@Bi_2MoO_6, it should be the consequence of p orbit of Bi being partially occupied by d orbit of loaded Pt, which leading the generation of new impurity level above the Fermi level of C@Bi_2MoO_6 [42,43]. From the E_g data and the E_{VB} positions, the possible band structure could be revealed (Fig. 4D). The pure Bi_2MoO_6 has an E_g of 2.2 eV between its valence band (3.2 eV vs. NHE) and conduction band (1.0 eV vs. NHE) (blue arrow in Fig. 4D). After carbon coating on the surface of the Bi_2MoO_6, hybrid carbon

might create a new valence band at 2.9 eV, which results in the narrow E_g of 1.9 eV in C@Bi_2MoO_6 structure (from 2.9 eV to 1.0 eV vs. NHE, black arrow in Fig. 4D) [44]. The supported Pt on the C@Bi_2MoO_6 causes a narrower E_g of 1.6 eV of the Pt/C@Bi_2MoO_6 composite, indicating the formation of a new hybrid conduction band at 1.3 eV (vs. NHE) composed by $Pt^{2+/4+}$ electron trap state [45–47]. It provides more efficient pathway to charges transformation with between the hybrid carbon state and the $Pt^{2+/4+}$ electron trap state (from 2.9 eV to 1.0 eV vs. NHE, orange arrow in Fig. 4D).

3.4. Photocatalytic activities and processes

The photocatalytic performance of the Pt/C@Bi_2MoO_6 composites is evaluated by the degradation of DBP solution under visible–light irradiation. The degradation curves (c/c_0) of DBP over the Pt/C@Bi_2MoO_6 composites with different Pt supported amount (Fig. 5A). Compared with Bi_2MoO_6, C@Bi_2MoO_6 and the controlled photolysis, the Pt/C@Bi_2MoO_6 composites show better DBP removal rate, and the c/c_0 of the 2.0%Pt/C@Bi_2MoO_6 composite is as low as 0.13, revealing the best photocatalytic performance among the Pt/C@Bi_2MoO_6 composites. The apparent quantum efficiency is a significant value in photocatalysis and represents the lower limits of the actual quantum
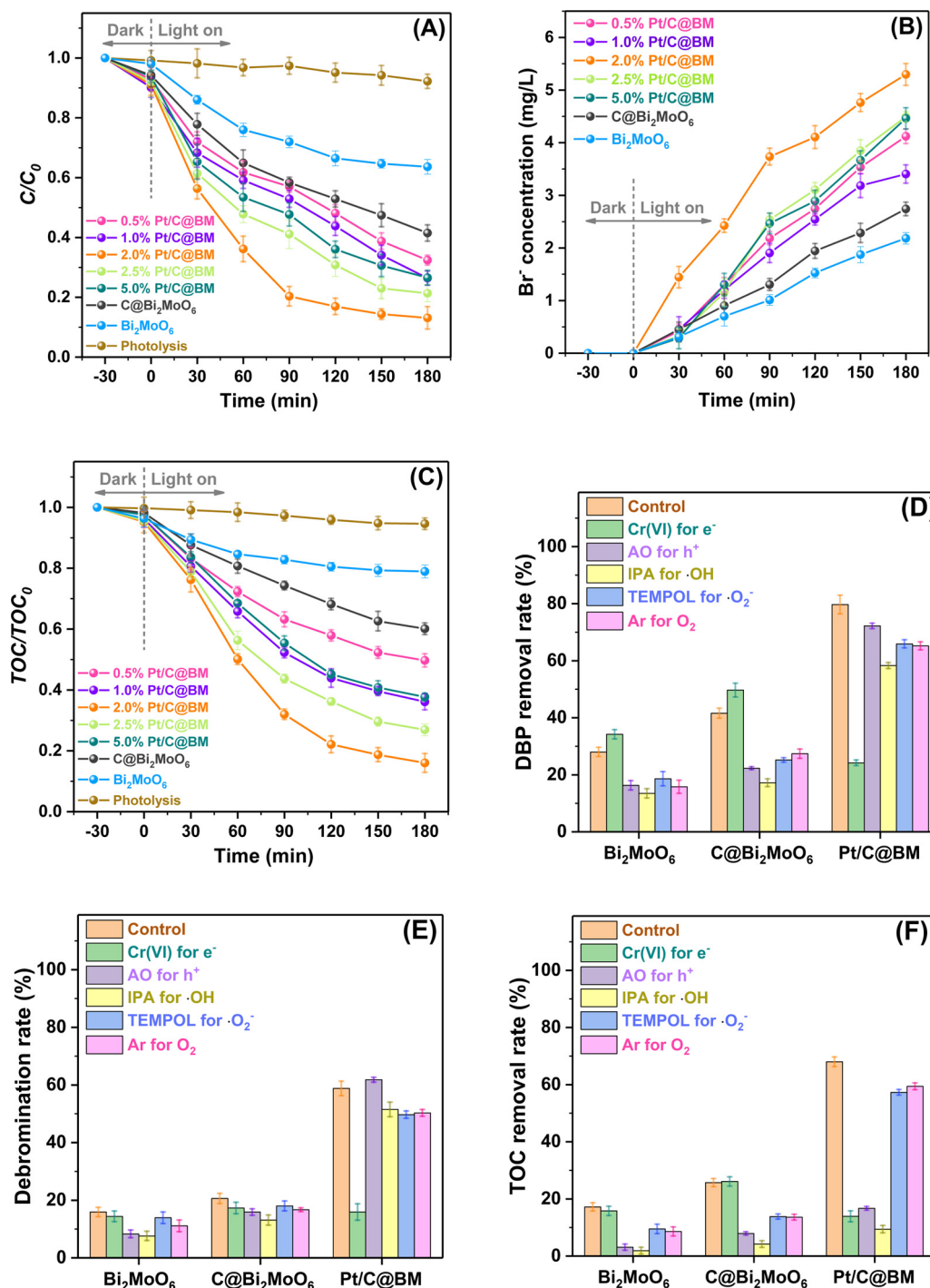
Fig. 5. (A) Photocatalytic degradation curves, (B) corresponding Br^- concentration, and (C) TOC removal curves during DBP degradation under visible light irradiation over pure Bi_2MoO_6, $C@Bi_2MoO_6$ and $Pt/C@Bi_2MoO_6$ (BM) composites, and effects of different scavengers on (D) DBP removal rate, (E) dechlorination rate and (F) TOC removal rate within 90 min irradiation under visible light. The photocatalyst dosage is 1.0 g/L, and DBP initial concentration is 10 mg/L.

yield [48,49]. The apparent quantum efficiency per electron of the DBP degradation by $Pt/C@Bi_2MoO_6$ is calculated as 3.86%, which is higher than that of DBP degradation by Bi_2MoO_6 (about 1.32%), indicating that the $Pt/C@Bi_2MoO_6$ composite has a lower charge carrier recombination rate than that of Bi_2MoO_6 photocatalyst [48]. The concentration of bromide ion ([Br^-]) was detected in the residual solution during the photodegradation of DBP (Fig. 5B). The theoretical [Br^-] in the solution is 6.35 mg/L if the DBP was entirely debrominated in the solution with the initial DBP concentration of 10 mg/L. The 2.0%Pt/C@Bi_2MoO_6 composite shows the highest debromination rate, and it

reaches 59% within 90 min photocatalytic degradation. Under 180 min irradiation with visible–light, about 83.5% bromine ions is removed from DBP to the solution (Fig. 5B), and about 13% bromine is remained in DBP molecule (Fig. 5A), and it can be calculated that about 3.5% bromine exists in the intermediate substances.

Furthermore, the TOC removal rate of the reaction solution during the DBP photodegradation was also measured to determinate the mineralization rate of DBP (Fig. 5C). The TOC removal rates (TOC/TOC_0) are slightly lower than the degradation rates (c/c_0) at each reaction time, suggesting that the majority of the DBP can be mineralized in the

photocatalytic process over the 2.0%Pt/C@Bi$_2$MoO$_6$ composite. With the irradiation of 180 min, it can be found that about 13% DBP is remained in the solution (Fig. 5A), and about 84% DBP is mineralized to inorganic substances as Br, CO$_2$ and H$_2$O (Fig. 5C), and we can conclude that about 3% DBP is decomposed to intermediate substances. The UV–Vis absorption spectra during the DBP photocatalytic degradation over the 2.0%Pt/C@Bi$_2$MoO$_6$ composite under visible light irradiation are shown in Fig. S2. The intensity of the maximum absorption band at 285 nm gradually decreased with increasing of reaction time and almost completely disappeared after 180 min irradiation. At the same time, no obvious peaks of intermediate substances appear in the action spectra, suggesting that most intermediate chromophoric groups are continuously degraded by Pt/C@Bi$_2$MoO$_6$ composite. According to the representative HPLC and MS spectra of DBP solution at different degradation time (Fig. S3), bromophenol and bromobisphenol are the major intermediate substances during the DBP photocatalytic degradation. It indicates that the debromination is the primary process in DBP degradation followed by mineralization. Dibromopentadiene is also detected in the solution, suggesting that coupling reactions and following decomposing behavior are also proceeded during the photocatalytic process [24].

The redox active species in the photocatalytic process are very important to reveal the mechanism of the photodegradation. We have detected the degradation rate (c/c_0), the debromination rate and the TOC removal rate (TOC/TOC$_0$) when capturing the photoexcited electron (e–) and hole (h$^+$), the dissolved oxygen (O$_2$), and the following secondary species ·OH, and ·O$_2$–. As shown in Fig. 5D, the DBP removal rates decrease when the oxidative species, such as h$^+$, ·OH and ·O$_2$–, are captured during the reaction of pure Bi$_2$MoO$_6$ and C@Bi$_2$MoO$_6$. It indicates that the oxidative species (h$^+$, ·OH and ·O$_2$–) are the main contributing ones rather than e– for removal of DBP over Bi$_2$MoO$_6$ and C@Bi$_2$MoO$_6$ photocatalysts. The same results are illustrated in the debromination rate and the TOC removal rate (Fig. 5E and F) in the presence of Bi$_2$MoO$_6$ and C@Bi$_2$MoO$_6$ photocatalysts. However, the Pt/C@Bi$_2$MoO$_6$ composite shows different results in the scavenger experiment. Significantly, the removal rates of DBP, Br– and TOC are decreased in the Pt/C@Bi$_2$MoO$_6$ composite system due to the e– being captured, suggesting that photoexcited e– has a great contribution to photodegradation process. In particular, capturing h$^+$ and ·OH causes obvious decrease in TOC removal rate, indicating that the mineralization of DBP mainly depends on the h$^+$ and ·OH species.

The photoluminescence (PL) spectrum of the photocatalyst is related to the transformation and separation of the photoexcited charge carries, and the PL signal is a direct evidence of the recombination of the photoexcited charges. Fig. 6A is the PL signals of the pure Bi$_2$MoO$_6$, C@Bi$_2$MoO$_6$ and Pt/C@Bi$_2$MoO$_6$ composite, and the spectrum of the Pt/C@Bi$_2$MoO$_6$ composite shows the lower peak intensity at 470 nm, suggesting its low recombination and high separation efficiencies between the photoexcited e– and h$^+$ pairs. The photoluminescence decay profiles can also reveal the recombination and transfer properties on the lifetime of the e– and h$^+$ pairs [50]. As shown in Fig. 6B, the dotted PL decay curves of the pure Bi$_2$MoO$_6$, C@Bi$_2$MoO$_6$ and Pt/C@Bi$_2$MoO$_6$ composite are fitted by function (1). Where $I(t)$ represents the PL intensity, A and τ are the relative weights of the decay components and the lifetimes corresponding to different recombination pathways, respectively. Furthermore, the average lifetime (τ_{ave}) can be calculated by function (2) [51].

$$I(t) = A_1 exp(-t/\tau_1) + A_2 exp(-t/\tau_1) \qquad (1)$$

$$\tau_{ave} = (A_1\tau_1 + A_2\tau_1)/(A_1 + A_2) \qquad (2)$$

The results reveals that the Pt/C@Bi$_2$MoO$_6$ composite shows relatively long lifetime (67.2 ns) of photoexcited charges, suggesting the higher separation efficiency between photoexcited e– and h$^+$ pairs than those of pure Bi$_2$MoO$_6$ (28.9 ns) and C@Bi$_2$MoO$_6$ (35.4 ns).

Further evidence for charge separation process can be found in the

photocurrent response and Nynquist plot of the electrochemical impedance spectrum (EIS) of the photocatalysts. We carry out the photocurrent measurement for pure Bi$_2$MoO$_6$, C@Bi$_2$MoO$_6$ and Pt/C@Bi$_2$MoO$_6$ composite (Fig. 6A). A uniform and fast response can be found with several on–off cycles in the three samples. The photocurrent of the Pt/C@Bi$_2$MoO$_6$ composite is about 1.5 and 3 times higher than those of pure Bi$_2$MoO$_6$ and C@Bi$_2$MoO$_6$, respectively, demonstrating that an enhanced charge separation of the Pt/C@Bi$_2$MoO$_6$ composite. From the EIS Nyquist plots (Fig. 6D), we can see that the Pt/C@Bi$_2$MoO$_6$ composite exhibits a smaller circular radius than the pure Bi$_2$MoO$_6$ and C@Bi$_2$MoO$_6$, demonstrating that the lifetime of the electrons and holes could be prolonged on the surface of the Pt/C@Bi$_2$MoO$_6$ composite.

The reactive oxygen species generated from the photoexcited process have been monitored by the electron spin resonance spectrum. As shown in Fig. 6E and F, the characteristic peaks of the DMPO–·OH and ·O$_2$– adducts are detected under visible–light irradiation. The intensity of the DMPO–·OH signals in the Pt/C@Bi$_2$MoO$_6$ composite are much stronger than those of pure Bi$_2$MoO$_6$ and C@Bi$_2$MoO$_6$. The distinguishing results can be seen in the spectra of DMPO–·O$_2$– signals, and no obvious DMPO–·O$_2$– signals could be found in all samples. It suggests that much–·O$_2$– could be generated on the surface of the Pt/C@Bi$_2$MoO$_6$ composite, indicating that ·OH radicals might provide much stronger oxidizability to decompose the organic pollutants.

3.5. Photocatalytic mechanism

It is well known that the photocatalytic performance is mainly governed by crystalline structure, adsorption ability, optical property and separation of photoexcited charges. The involvement of carbon layer reported a slightly influence on Bi$_2$MoO$_6$ phase structure with previous work [52]. Analysis of XRD data showed a decreasing intensity of Bi$_2$MoO$_6$ crystalline followed by Pt supported, indicating that these changes would not induce the improvement of photocatalytic performance. Compared with pure Bi$_2$MoO$_6$, the adsorption ability of modified Pt/C@Bi$_2$MoO$_6$ composite showed similar adsorption capacity within the dark adsorption of DBP process (Fig. 5A), demonstrating that the adsorption ability was not the dominant factor in enhancing photocatalytic activity of Pt/C@Bi$_2$MoO$_6$ composite. Therefore, remarkably high photocatalytic activity of Pt/C@Bi$_2$MoO$_6$ composite should be attributed to the excellent optical property (Fig. 4) and high separation efficiency of charges (Fig. 6).

The energy band of Bi$_2$MoO$_6$ is consist of Bi 6s and O 2p electronic orbital, acting as valence band (VB) and conduction band (CB), respectively [31]. As carbon layer coated on the surface of Bi$_2$MoO$_6$, a new impurity energy level will be formed by hybridization of Bi 6s and C 1s, which is so–called highest occupied molecular orbital (HOMO) [53,54]. The new HOMO level shows a high position of +2.9 eV vs. NHE (Fig. 4D), confirmed by analysis of the valence band XPS spectra (Fig. 4C) of C@Bi$_2$MoO$_6$ and Pt/C@Bi$_2$MoO$_6$ composite. Additionally, our measurements of band gap energy (E_g) values showed similar transformation in the CB of Bi$_2$MoO$_6$. The lowest unoccupied molecular orbital (LUMO) position (+1.3 eV vs. NHE) of the Pt/C@Bi$_2$MoO$_6$ composite can obtained by its band gap energy and HOMO level position (Fig. 4D), which is below the CB of Bi$_2$MoO$_6$. We assume that the transformation of the new LUMO level is assigned to the orbital hybridization of O 2p and Pt 4f (Fig. 4D). Thus, the data suggest that the new HOMO and LUMO levels provide a narrower band gap to be excited by lower optical energy, indicating the significant enhancement of visible–light utilization efficiency.

The oxidation ability of CB in semiconductor is considered as the formation of ·O$_2$– by reaction of oxygen and electrons. The LUMO level position (+1.3 eV vs. NHE) of the Pt/C@Bi$_2$MoO$_6$ composite in our study is higher than that of O$_2$/·O$_2$– transformation (–0.046 eV, vs. NHE) [55], suggesting that ·O$_2$– should not be generated in the CB of the Pt/C@Bi$_2$MoO$_6$ composite, which is confirmed by the ESR spectra (Fig. 6F) and the scavenger results (Fig. 5). As O$_2$ and ·O$_2$– were
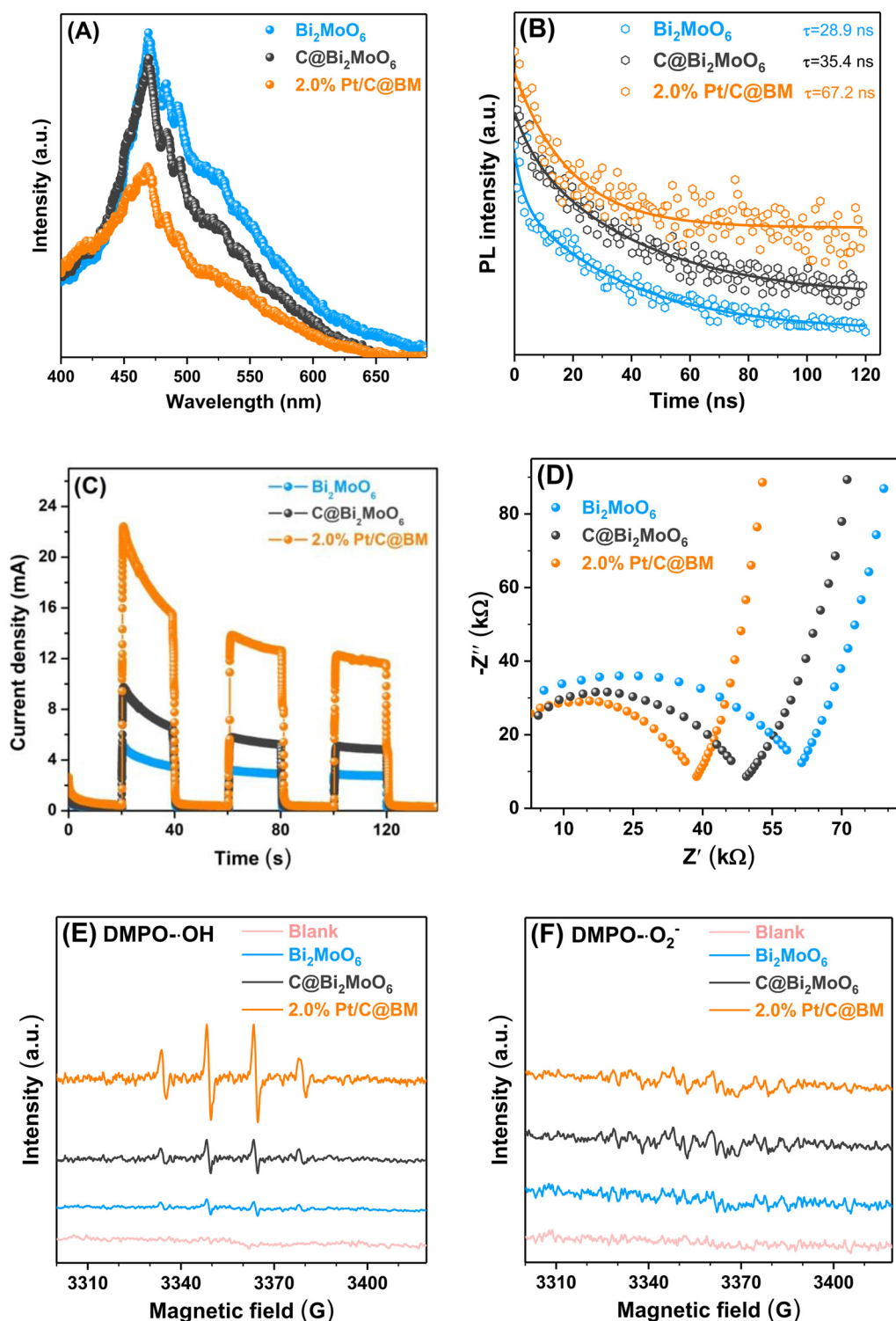
Fig. 6. (A) PL spectra, (B) PL decay measurements, (C) transient photocurrent responses, (D) EIS Nyquist plots, and (E, F) ESR spectra of ·OH and ·O_2– trapped by DMPO of the pure Bi_2MoO_6, $C@Bi_2MoO_6$ and $Pt/C@Bi_2MoO_6$ (BM) composites.

captured by scavengers, the DBP removal rate, debromination rate and TOC removal rate had no obvious changes, illustrating that there were few ·O_2– being generated. However, distinctive results could be found in electron scavenger process (Fig. 5), indicating that electrons are among the most effective species being involved in DBP degradation. The accumulated electrons in the CB of the $Pt/C@Bi_2MoO_6$ composite have strongly reductive activity to bombard the C−Br bonds in DBP molecular structure to produce bromine ions (Br–) into the solution,

and the formation of electric field by the plasmonic effect of Pt° atoms significantly accelerate the electrons accumulation process and following debromination procedure [56,57]. Therefore, the supported Pt can form a new LUMO level by oxidized $Pt^{2+/4+}$ as well as generate reductive active site in plasma electron field of the Pt° atoms, which increases the optical utilization and electron reduction activity to enhance the DBP photodegradation.

On the other side, the electrons transition from new HOMO level
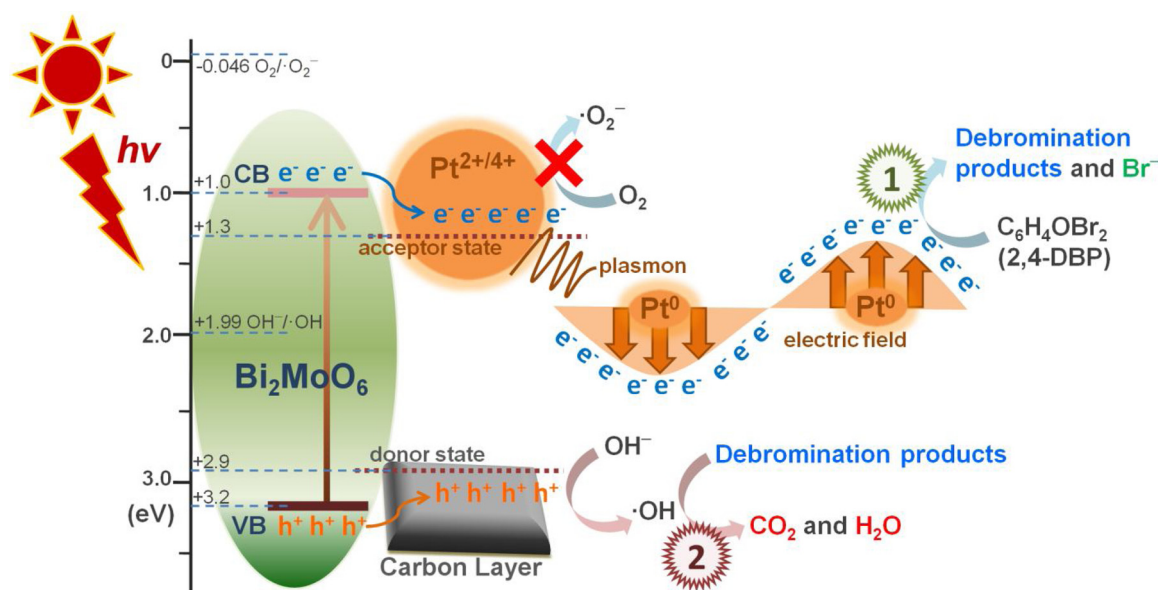
Scheme 2. Schematic presentation illustrating charge generation and transfer procedure over the Pt/C@Bi$_2$MoO$_6$ composite combined with conjectural photocatalytic degradation of DBP mechanism.
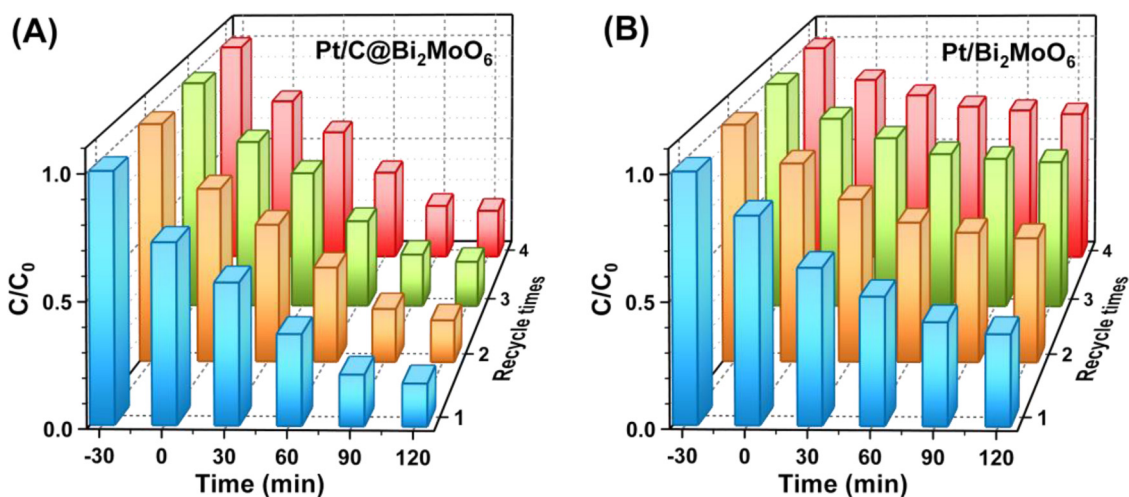

Fig. 7. Recycling tests of (A) 2.0%Pt/C@Bi$_2$MoO$_6$ and (B) 2.0%Pt/Bi$_2$MoO$_6$ composite under visible light irradiation by degradation of DBP. The photocatalyst dosage is 1.0 g/L, and DBP initial concentration is 10 mg/L.

proceeds accumulation of holes, followed by ·OH species. The debromination rate has no obvious change by capturing of holes or ·OH species (Fig. 5E), suggesting that the oxidized species (hole or ·OH) have almost not affected the debromination process. Furthermore, the oxidized species are dominantly attributed to the TOC removal according to the scavenger experiment (Fig. 5F). Thus, the data show that the debromination and oxidization processes are occurred in CB and VB of the Pt/C@Bi$_2$MoO$_6$ composite, respectively, and the possible mechanism of the photocatalytic degradation of DBP is illustrated in Scheme 2. As the reaction proceeds under visible–light irradiation, increasing amount of photoexcited electrons and holes are generated at the acceptor state of CB and donor state of VB on the surface of the Pt/C@Bi$_2$MoO$_6$ composite, respectively. The next process of photocatalytic degradation of DBP could be in two steps: debromination and oxidization, in which debromination is the primary and control procedure. Firstly, the accumulated electrons in the CB, especially in the electric field formed by the plasmonic effect of Pt° atoms significantly accelerate the electrons accumulation process and following debromination procedure. The DBP (C$_6$H$_4$OBr$_2$) could be reduced by electron bombardment, and monobrominated and non–brominated intermediate

products (e.g. bromophenol, bromobisphenol) would be produced. Based on the debromination procedure, subsequent oxidization procedure of the intermediate products by holes and ·OH would be occurred in the VB of the Pt/C@Bi$_2$MoO$_6$ composite, and finally, the DBP could be mineralized to harmless CO$_2$ and H$_2$O. The generated bromide ions are harmful to the environment, and it would be further treated by chemical or physicochemical methods [58].

Stability of the Pt/C@Bi$_2$MoO$_6$ composite was measured by recycling test for four times (Fig. 7A), and the activity of the composite has no obvious change at the fourth usage, suggesting that the Pt/C@Bi$_2$MoO$_6$ composite has a stable property under visible–light irradiation in reaction solution. For comparison, the recycling test of the Pt/Bi$_2$MoO$_6$ composite was simultaneously measured (Fig. 7B). It could be found that in absence of carbon layer, the Pt/Bi$_2$MoO$_6$ composite shows a decreasing DBP degradation rates for four recycling test, indicating that the carbon layer plays an important role in stability of the composite to form a tightly bind with Pt on the surface.

4. Conclusions

The Pt supported and carbon coated Bi_2MoO_6 composite has been synthesized and proved to be more efficient and reliable in DBP photocatalytic degradation under visible–light irradiation. Pt and carbon layer can tightly bind to the surface of Bi_2MoO_6 with the formation of $C-O-Bi$ and $C-O-Pt$ bonds. Pt and carbon can hybrid the original energy band structure to generate new impurity levels to enhance the visible–light utilization efficiency. The supported Pt can form a new LUMO level by oxidized $Pt^{2+/4+}$ as well as generate reductive active site in plasma electron field of the Pt° atoms. The carbon layer improves the photocatalytic performance for three reasons of formation of new HOMO level, transformation electron by excellent conductivity, and immobilization of Pt on the surface of the composite. The debromination procedure of DBP starts by electron in the CB in priority to generate non–brominated intermediate products, and then the oxidization and mineralization procedures proceed to finish the complete degradation of DBP. This research reveals the roles of carbon layer and Pt in the Pt/C@Bi_2MoO_6 composite, exhibiting a new route to design an efficient and stable photocatalyst and a feasible method for persistent organic pollutant treatment.

Appendix A. Supplementary data

Supplementary material related to this article can be found, in the online version, at doi:https://doi.org/10.1016/j.apcatb.2018.06.016.

References

[1] H.B. Cheng, S. Keith, C.A. Paul, Electrochim. Acta 49 (2004) 729–735.
[2] P.L. Maria, A.I. Balabanovich, J. Anal. Appl. Pyrol. 90 (2011) 63–71.
[3] G.Y. Li, J.K. Xiong, P.K. Wong, T.C. An, Environ. Pollut. 208 (2016) 796–802.
[4] A. Bhatnagar, J. Hazard. Mater. 139 (2007) 93–102.
[5] W.Y. Pang, J. Jiang, Y. Gao, Y. Zhou, X.L. Huangfu, Y.Z. Liu, J. Ma, Environ. Sci. Technol. 48 (2014) 615–623.
[6] D.D. Xu, X.Z. Song, W.Z. Qi, H. Wang, Z.Y. Bian, Chem. Eng. J. 333 (2018) 477–485.
[7] Q.Q. Zhu, M. Igarashi, M. Sasaki, T. Miyamoto, R. Kodama, M. Fukushima, Appl. Catal. B: Environ. 183 (2016) 61–68.
[8] S.W. Gao, C.S. Guo, S. Hou, L. Wan, Q. Wang, J.P. Lv, Y. Zhang, J.F. Gao, W. Meng, J. Xu, J. Hazard. Mater. 331 (2017) 1–12.
[9] H. Khan, M.G. Rigamonti, G.S. Patience, D.C. Boffito, Appl. Catal. B: Environ. 226 (2018) 311–323.
[10] E. Kusvuran, A. Samil, O.M. Atanur, O. Erbatur, Appl. Catal. B: Environ. 58 (2005) 211–216.
[11] B. Gao, L.F. Liu, J.D. Liu, F.L. Yang, Appl. Catal. B: Environ. 147 (2014) 929–939.
[12] M. Aslam, M.T. Qamar, M.T. Soomro, I.M.I. Ismail, N. Salah, T. Almeelbi, M.A. Gondal, A. Hameed, Appl. Catal. B: Environ. 180 (2016) 391–402.
[13] M.T. Qamar, M. Aslam, Z.A. Rehan, M.T. Soomro, J.M. Basahi, I.M.I. Ismail, T. Almeelbi, A. Hameed, Appl. Catal. B: Environ. 201 (2017) 105–118.
[14] L.K. Lee, C. Ding, K.L. Yang, J.Z. He, Environ. Sci. Technol. 45 (2011) 8475–8482.
[15] D. Kim, J.R. Chen, T.F. Yen, J. Hazard. Mater. 163 (2009) 231–238.
[16] M.Y. Ahn, T.R. Filley, C.T. Jafvert, L. Nies, I. Hua, J. Bezares-Cruz, Environ. Sci. Technol. 40 (2006) 215–220.
[17] G.P. Gao, Y. Jian, E.R. Waclawik, A.J. Du, J. Am. Chem. Soc. 138 (2016) 6292–6297.
[18] M.J. Li, Z.B. Yu, Q. Liu, L. Sun, W.Y. Huang, Chem. Eng. J. 286 (2016) 232–238.
[19] A. Tanaka, K. Hashimoto, H. Kominami, J. Am. Chem. Soc. 136 (2014) 586–589.
[20] Y.Y. Sun, J. Wu, T.J. Ma, P.C. Wang, C.Y. Cui, D. Ma, Appl. Surf. Sci. 403 (2017) 141–150.
[21] T.J. Ma, J. Wu, Y.D. Mi, Q.H. Chen, D. Ma, C. Chai, Sep. Purif. Technol. 183 (2017) 54–65.
[22] D. Ma, J. Wu, M.C. Gao, Y.J. Xin, Y.Y. Sun, T.J. Ma, Chem. Eng. J. 313 (2017) 1567–1576.
[23] D. Ma, J. Wu, M.C. Gao, Y.J. Xin, C. Chai, Chem. Eng. J. 316 (2017) 461–470.
[24] H.X. Zhao, J.Q. Jiang, Y.L. Wang, H.J. Lehmler, G.R. Buettner, X. Quan, J.W. Chen, Environ. Sci. Technol. 49 (2015) 14120–14128.
[25] D. Ma, Y.J. Xin, M.C. Gao, J. Wu, Appl. Catal. B: Environ. 147 (2014) 49–57.
[26] D. Ma, J. Wu, M.C. Gao, Y.J. Xin, T.J. Ma, Y.Y. Sun, Chem. Eng. J. 290 (2016) 136–146.
[27] L.W. Zhang, T.G. Xu, X. Zhao, Y.F. Zhu, Appl. Catal. B: Environ. 98 (2010) 138–146.
[28] J.J. Xue, S.S. Ma, Y.M. Zhou, Z.W. Zhang, M. He, ACS Appl. Mater. Interfaces 18 (2015) 9630–9637.
[29] S.H. Zhou, B. Varughese, B. Eichhorn, G. Jackson, K. McIlwrath, Angew. Chem. 117 (2005) 4615–4619.
[30] G.T. Fu, L.F. Ding, Y. Chen, J. Lin, Y.W. Tang, T.H. Lu, CrystEngComm 16 (2014) 1606–1610.
[31] Z. Dai, F. Qin, H.P. Zhao, J. Ding, Y.L. Liu, R. Chen, ACS Catal. 6 (2016) 3180–3192.
[32] H.P. Li, J.Y. Liu, W.G. Hou, N. Du, R.J. Zhang, X.T. Tao, Appl. Catal. B: Environ. 160–161 (2014) 89–97.
[33] J. Di, J.X. Xia, M.X. Ji, H.P. Li, H. Xu, H.M. Li, R. Chen, Nanoscale 7 (2015) 11433–11443.
[34] A. Phuruangrat, P. Jitrou, P. Dumrongrojthanath, N. Ekthammathat, B. Kuntalue, S. Thongtem, T. Thongtem, J. Nanomater. 2013 (2013) 8.
[35] L.W. Zhang, H.Y. Cheng, R.L. Zong, Y.F. Zhu, J. Phys. Chem. C 113 (2009) 2368–2374.
[36] X.C. Meng, Z.S. Zhang, J. Catal. 344 (2016) 616–630.
[37] H.J. Lu, L.L. Xu, B. Wei, M.Y. Zhang, H. Gao, W.J. Sun, Appl. Surf. Sci. 303 (2014) 360–366.
[38] F. Wang, Y. Jiang, D.J. Lawes, G.E. Ball, C. Zhou, Z. Liu, R. Amal, ACS Catal. 5 (2015) 3924–3931.
[39] Y.R. Yang, P. Gao, X.C. Ren, L.N. Sha, P.P. Yang, J.J. Zhang, Y.J. Chen, L. Yang, Appl. Catal. B: Environ. 218 (2017) 751–757.
[40] H. Pan, Y.P. Feng, Q.Y. Wu, Z.G. Huang, J.Y. Lin, Phys. Rev. B 77 (2008) 125211.
[41] S.Y. Wang, X. Ding, X.H. Zhang, H. Pang, X. Hai, G.M. Zhan, W. Zhou, H. Song, L.Z. Zhang, H. Chen, J.H. Ye, Adv. Funct. Mater. 27 (2017) 1703923.
[42] J. Deng, H.B. Li, J.P. Xiao, Y.C. Tu, D.H. Deng, H.X. Yang, H.F. Tian, J.Q. Li, P.J. Ren, X.H. Bao, Energy Environ. Sci. 8 (2015) 1594–1601.
[43] V. Subramanian, E.E. Wolf, P.V. Kamat, J. Phys. Chem. B 107 (2003) 7479–7485.
[44] G. Mamba, A.K. Mishra, Appl. Catal. B: Environ. 198 (2016) 347–377.
[45] G.P. Gao, Y. Jiao, E.R. Waclawik, A.J. Du, J. Am. Chem. Soc. 138 (2016) 6292–6297.
[46] X.G. Li, W.T. Bi, L. Zhang, S. Tao, W.S. Chu, Q. Zhang, Y. Luo, C.Z. Wu, Y. Xie, Adv. Mater. 28 (2016) 2427–2431.
[47] Z.K. Zheng, B.B. Huang, X.Y. Qin, X.Y. Zhang, Y. Dai, M.H. Whangbo, J. Mater. Chem. 21 (2011) 9079–9087.
[48] R.A. Doong, W.H. Chang, J. Photochem. Photobiol. A 107 (1997) 239–244.
[49] H.M. Coleman, B.R. Eggins, J.A. Byrne, F.L. Palmer, E. King, Appl. Catal. B: Environ. 24 (2000) L1–L5.
[50] J.L.Q. Song, T.T. Jiang, T.Y. Guo, L. Liu, H.J. Wang, T.Y. Xia, W.T. Zhang, X.C. Ye, M.Y. Yang, L.X. Zhu, R.X. Xia, X.L. Xu, Inorg. Chem. 54 (2015) 1627–1633.
[51] G. Gong, Y.H. Liu, B.D. Mao, L.L. Tan, Y.L. Yang, W.D. Shi, Appl. Catal. B: Environ. 216 (2017) 11–19.
[52] C.Y. Su, Y.C. Hsueh, C.C. Kei, C.T. Lin, T.P. Perng, J. Phys. Chem. C 117 (2013) 11610–11618.
[53] L.W. Zhang, H.B. Fu, Y.F. Zhu, Adv. Funct. Mater. 18 (2008) 2180–2189.
[54] J. Chen, F. Zhang, Y.L. Zhao, Y.C. Guo, P.J. Gong, Z.Q. Li, H.S. Qian, Appl. Surf. Sci. 362 (2015) 126–131.
[55] D. Ma, Y.X. Zhang, M.C. Gao, Y.J. Xin, J. Wu, N. Bao, Appl. Surf. Sci. 353 (2015) 118–126.
[56] C.C. Nguyen, D. Nguyen, T. OnDo, Appl. Catal. B Environ. 226 (2018) 46–52.
[57] V. Sharma, S. Kumar, V. Krishnan, Mater. Chem. Phys. 179 (2016) 129–136.
[58] L. Ding, H.P. Deng, C. Wu, X. Han, Chem. Eng. J. 181–182 (2012) 360–370.